Influence of snowpack properties and local incidence angle on SAR signal depolarization: a mathematical model for high-resolution snow depth estimation

Alberto Mariani[1,2,*], Jacopo Borsotti[3,†], Franz Livio[2,‡], Giacomo Villa[1,§],
Martin Metzger[1,¶], Fabiano Monti[1,∞]
[1]Alpsolut S.r.l., Via Saroch 1098/a, 23041 Livigno, Italy
[2]University of Insubria, Department of Science and High Technology,
Via Valleggio 11, 22100 Como, Italy
[3]University of Parma, Department of Mathematical, Physical and Computer Sciences,
Parco Area delle Scienze 53/A, 43124 Parma, Italy
[*]mariani@alpsolut.eu (corresponding author), [†]jacopo.borsotti@unipr.it,
[‡]franz.livio@uninsubria.it, [§]villa@alpsolut.eu, [¶]metzger@alpsolut.eu, [∞]monti@alpsolut.eu

Keywords: Synthetic Aperture Radar, Snow depth retrieval, Local incidence angle, DpRVIc, Avalanche forecasting, Signal depolarization

Abstract. Recently, Dual-Polarimetric Synthetic Aperture Radar (SAR) has been shown to be effective for large-scale snow cover monitoring, but it faces significant challenges when applied to finer resolutions, which are crucial for applications such as avalanche forecasting. In this study, we propose a novel mathematical model to retrieve snow properties from Sentinel-1 SAR data, leveraging variations in the Dual-Polarimetric Radar Vegetation Index ($DpRVI_c$). We introduce the Snow Index SAR ($SIsar$), which quantifies variations in signal depolarization occurring within the snowpack. Our study, conducted in the Central Italian Alps, reveals a strong correlation between the $SIsar$ index and the snowpack height, enabling accurate snow depth estimation. We also demonstrate the significant impact of the local incidence angle on signal depolarization during the accumulation season. Based on this, we derive a mathematical correction for the incidence angle, whose inclusion in the model reduces snow depth estimation errors by approximately 39 %. The model validation conducted in Tromsø, Norway, confirms its applicability beyond the calibration area, with a root mean squared error (RMSE) of 30.7 cm and a mean absolute error (MAE) of 24.3 cm. These findings enhance our understanding of dual-polarimetric Sentinel-1 SAR data sensitivity for high-resolution snow monitoring, providing valuable insights for avalanche forecasting and hydrological applications.

1 Introduction

Snow, in addition to being a complex meteorological phenomenon, represents one of the main resources of the mountain environment, and it is well-established that more than one-sixth of the Earth's population relies on glaciers and seasonal snowpack for their water supply (Barnett et al., 2005). Moreover, this water source is released gradually during the spring and summer season, filling rivers and lakes, allowing the production of hydroelectric power (80 % of Alpine waterways are exploited by hydroelectric power plants) and, above all, renewing the groundwater reserves essential for drinking water supply and agriculture (Soncini and Bocchiola, 2011). Furthermore, one of the fields most interested in snow monitoring is avalanche forecasting, since snow avalanches are among the most significant hazards in mountain regions, causing approximately 100 fatalities in Europe alone each winter (EAWS, 2025). While for environmental purposes the study of snow at the large-scale is essential (i.e., from a single mountain range to the entire globe), for avalanche forecasting purposes there is more interest in the distribution and properties of the snowpack at the small-scale (i.e., from an individual slope to a single mountain massif; Mariani et al. (2023)). In recent years, satellite remote sensing has become a fundamental tool for monitoring snow cover properties at the large-scale, particularly in remote regions lacking monitoring stations (Awasthi and Varade, 2021). One of the most important snow properties that can be monitored using remote sensing techniques is the snowpack height (HS). In this study, we propose a new mathematical model for estimating HS using dual-polarimetric Synthetic Aperture Radar

(SAR) data, which corrects biases inherent in previous methods, thereby improving the retrieval of HS at the small-scale.

Initially, optical satellite data with medium resolution, such as Moderate-Resolution Imaging Spectroradiometer (MODIS), Advanced Very High-Resolution Radiometer (AVHRR), and Sentinel-2, served as the primary spaceborne data sources for monitoring snow cover extent and surface properties (Feng et al., 2024). However, optical imaging has significant limitations: it cannot provide information under cloud cover or during nighttime and is sensitive only to the surface of the snowpack. To overcome these limitations, the use of SAR data has been widely explored since the first studies demonstrated that the SAR signal interacts with snow as a volume (Tsai et al., 2019). The interaction of SAR signals with snow is primarily governed by its dielectric constant, which depends on several snowpack parameters and on the microwave frequency (Snehmani et al., 2015). The presence of liquid water in the snowpack significantly affects SAR backscatter, making wet snow retrieval one of the primary applications of SAR related to snow monitoring. Key contributions in this field include the works of Nagler and Rott (2000) and Nagler at al. (2016). Additionally, SAR satellites are increasingly used to detect avalanche deposits, providing crucial data for avalanche forecasting (Kapper at al., 2023). At the frequencies commonly used for snow monitoring in SAR missions, such as X-band and C-band, the radar signal penetrates a dry snowpack (i.e., a snowpack without liquid water), reaching the underlying soil and leading to surface backscatter, which predominantly contributes to the total received signal (Awasthi and Varade, 2021). However, a certain amount of volume backscatter is also generated within the snowpack, leading to an increase in the received signal compared to the bare soil, particularly in cross polarization (Chang et al., 2014). This snowpack volumetric backscatter production is significant especially at high-frequency (i.e., Ku-band), where the influence of the underlying soil is limited (Tsang et al., 2022). Despite this, high-resolution Ku-band satellite products are currently unavailable, and new missions, such as the European Space Agency (ESA) Cold Regions Hydrology High-resolution Observatory (CoReH2O; Rott et al. (2012)), have not been selected for implementation. In Pettinato et al. (2013), the potential of COSMO-SkyMed X-band SAR for HS retrieval was demonstrated, highlighting the capability of a radiative transfer model to simulate snowpack backscatter at this frequency. To overcome the difficulties in neglecting the underlying soil contribution to the total backscatter at low-frequency SAR platforms, Reppucci et al. (2012) utilized polarimetric decomposition of full-polarimetric RADARSAT-2 products (C-band) to extract the volumetric backscatter contribution and retrieve snowpack characteristics. However, both X-band and quad-polarimetric products are largely confined to commercial platforms, therefore several studies have focused on exploring the use of freely available Sentinel-1 imagery. In Lievens et al. (2019), the separation of ground and snowpack contributions to the total backscatter in dual-polarimetric Sentinel-1 products was achieved by computing the ratio between the cross-polarization channel (VH), which is more sensitive to volumetric backscatter, and the co-polarization channel (VV), which is more sensitive to the surface backscatter produced at the snow-soil interface. The resulting index was then used to map HS at 1 km and 500 m resolution over the European Alps in Lievens et al. (2022). Moreover, Feng et al. (2024) recently demonstrated that the dual-polarimetric radar vegetation index ($DpRVI_c$) outperforms all other dual-polarimetric indices recoverable from Sentinel-1 in HS retrieval. This index describes an approximation of the degree of depolarization of the backscattered signal, and theoretically ranges from 0, indicating no depolarization, to 1, representing full depolarization of the signal (Mandal et al., 2020). Full signal depolarization is theoretically obtained when the intensity of the cross-polarized band equals the intensity of the co-polarized band. Since snowpack volumetric backscatter causes signal depolarization, the $DpRVI_c$ index increases as HS increases, and its ability in snow depth estimation is demonstrated for the Scandinavian Alps. Further progress in understanding the backscatter mechanisms of the snowpack in response to Sentinel-1's C-band signal, as well as the sensitivity of derived polarimetric indices and interferometric coherence to seasonal snow accumulation, is presented in Jans et al. (2025). The cited study also analyzes the influence of the incidence angle between the SAR signal and the normal to the slope surface, known as the local incidence angle (LIA), on HS and on the snow water equivalent (SWE) sensitivity, at a resolution of 1 km, over the Alps. However, despite the significant progress made in leveraging SAR data to monitor snowpack properties at large-scales, limited attention has been given to smaller-scale investigations. Studies targeting specific mountain ranges, valleys, or avalanche forecasting zones where a resolution at the scale of the individual slope is required, are still scarce.

The aim of the present work is to analyze in greater detail the capability of the $DpRVI_c$ index for snow depth, and other snowpack properties, retrieval at the small-scale. To this end, we compute a snow index based on $DpRVI_c$ variations, taking as reference its summer average value, here named

Snow Index SAR (*SIsar*). We examine the relationship between the *SIsar* index and measured or simulated snowpack properties for two proximal locations in the Central Italian Alps. The snowpack is a highly dynamic material that undergoes several metamorphic processes throughout the season, altering its physical and mechanical properties (McClung and Schaerer, 2023). For this reason, we try to identify which snowpack variables are more correlated to SAR signal depolarization variations, described by the *SIsar* index. Additionally, the complex mountain topography, combined with the side-looking geometry of SAR, causes significant variation in the *LIA* at the small-scale. We hypothesize that as the *LIA* increases, the SAR signal penetrates more snow, leading to greater depolarization at the slope-scale. Therefore, we analyze in detail the influence of the *LIA* on the *SIsar* index. Based on this analysis, we propose a novel mathematical model to estimate *HS*, demonstrating a significant improvement resulting from considering the *LIA*. The model is validated with in situ observations collected in an area around Tromsø, Norway, which is significantly different from the calibration area in terms of snow and weather conditions.

2 Study areas and data

2.1 Study areas

We considered two study areas: the model calibration area and the model validation area. The model calibration area is located around the municipality of Livigno (Sondrio province, Italy), on the border with Switzerland in the central Rhaetian Alps (46°28′ N, 10°8′ E; see Figure 1). The elevation ranges from 1800 m asl on the Livigno valley floor to 4049 m asl at the summit of Piz Bernina. The area experiences an Alpine climate, with snow regimes transitioning from continental in the northern part and maritime in the southern region (McClung and Schaerer, 2023). The Livigno valley floor is predominantly anthropogenic, with a ski area occupying both sides of the valley up to 2800 m asl. The higher alpine regions are mainly covered by alpine meadows and talus, with widespread permafrost present (Dramis and Gugliemin, 2001). In the southwestern part of the area, numerous alpine glaciers can be found. The intense tourist activity in the area, particularly among winter outdoor enthusiasts, has led to the development of a local avalanche forecasting system, and several automatic weather stations (AWSs) equipped with standard gauges are operational (Monti et al., 2014). The model validation area is located around Tromsø, Norway (69°38′58″ N 18°57′25″ E). This region is characterized by an Arctic transitional snow climate (Velsand, 2017), and features relatively smoother topography compared to the Alpine area used for model calibration.

To analyze the evolution of the SAR signals over the seasons and their dependency on the snowpack properties, we selected two sampling areas inside the model calibration area (hereafter referred to as regression sampling areas) around two AWSs: Gessi (46°31′23″ N, 10°7′27″ E – 2633 m asl) and Vall (46°28′37″ N, 10°11′28″ E – 2660 m asl). Both areas were defined with a 50 m buffer around the locations of the AWSs, which was adjusted to exclude zones affected by wind deposition and erosion, while aiming to keep the morphology as homogeneous as possible. Both regression sampling areas have slopes ranging from 0° to 12°, with the AWSs located on flat terrain, and a predominant north-west slope orientation. To analyze the relationship of SAR signal variations with the *LIA*, we selected two larger areas around the location of the AWSs (hereafter referred to as *LIA* sampling areas) to ensure a heterogeneous *LIA* distribution. For these areas, a 4 km buffer was applied around the location of the AWSs, with elevation differences limited to ±200 m. Zones with anthropogenic features, such as ski slopes or zones where snow cover is heavily influenced by ski touring and freeride tracks, were excluded based on experts' experience. It is important to note that the regression sampling areas and the *LIA* sampling areas were independent.

To validate the results, we selected a 50 × 50 km area inside the model validation area where in situ measurements were available. Within this area, we applied a 50 m buffer around each measurement location to sample the model estimations (hereafter referred to as validation sampling areas).

2.2 SAR data

In the present study, we employed freely available level-1 GRD data products from the Sentinel-1 platform, which provides data from a dual-polarization C-band Synthetic Aperture Radar (SAR) instrument at 5.405 GHz. The data were acquired in Interferometric Wide swath mode (IW), with an original resolution of 5 m in range and 20 m in azimuth. Both VV and VH polarization were available, and the platform was right-looking. During the SAR data preprocessing phase, as well as to compute the local incidence angle for the two AGs, we used the freely-available Copernicus GLO-30 DEM with a 30 m cell resolution (European Union, 2021).

For the study and the calibration of our model we selected two acquisition geometries (AGs) that entirely cover the calibration area, taking advantage of the different acquisition times and look directions. The first AG, with relative orbit number 168, was in the ascending direction and was

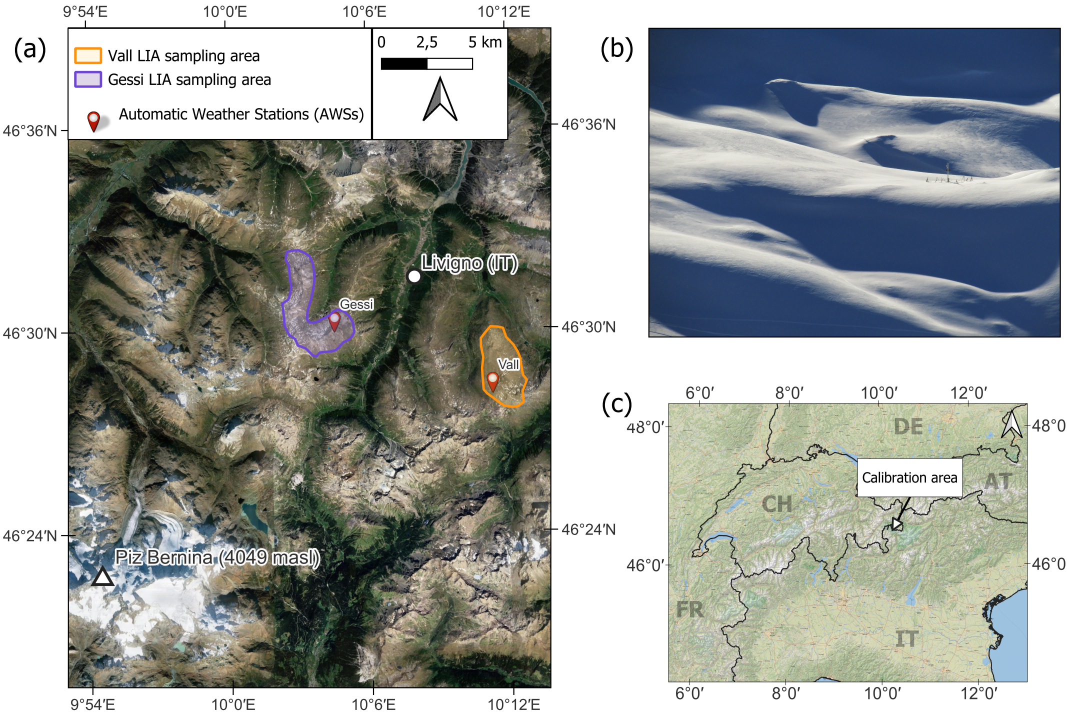

Figure 1: Spatial framework of the model calibration area. (a) General overview of the area together with the locations of the AWSs and the LIA sampling areas. (b) Picture of the Gessi AWS acquired in winter 2023-2024, HS was approximately 180 cm, the height of the station is around 3 m. (c) Geographic location of the area within the Alpine chain.

acquired around 5 a.m. UTC. The second orbit, with relative orbit number 15, was in the descending direction and acquired around 5 p.m. UTC. The different acquisition times provided valuable information for monitoring snowpack conditions, which could vary significantly between morning and afternoon at this latitude. In the present study, we focused on the period from October 2022 to July 2024, covering two full snow seasons. Given the Sentinel-1 revisit time of 12 days, a total number of 57 ascending plus 59 descending Ground Range Detected (GRD) products were downloaded in Cloud Optimized Geotiff format (COG).

For the validation of the model we downloaded Sentinel-1 GRD products over the validation area for the months of December 2024 and January 2025. The two AGs had relative orbit numbers 131, with ascending direction and acquisition time around 5 a.m. UTC, and 95, with descending direction and acquisition time around 5 p.m. UTC.

2.3 Weather and snowpack measurements

Concerning the calibration area, the weather data utilized to run the snowpack evolution model were collected by the two AWSs, which operated throughout the analysis period. These measurements included air and snow surface temperatures, snowpack height, relative humidity, wind velocities, and incoming shortwave radiation. It should be noted that these AWSs are routinely employed for snowpack simulations to support avalanche forecasting within the Livigno municipality (additionally, standard in situ snow stratigraphies are routinely performed in the backcountry areas to calibrate model parameters and validate simulation outputs; Monti at al. (2016)). During the 2022-2023 winter season, meteorological conditions were marked by below-average precipitation. The maximum HS recorded at the Vall station was 146 cm on April 22, 2023. Field observations revealed that the combination of low temperatures and reduced snowpack thickness led to significant constructive metamorphism, resulting in a generally low-density snowpack dominated by depth hoar and faceted grains in the deeper layers (McClung and Schaerer, 2023). In contrast, the 2023-2024 winter season experienced frequent Atlantic weather systems, leading to above-average temperatures and precipitation. The maximum HS during this period was 322 cm, recorded at the Vall station on April 3, 2024. These conditions produced a dense and warm snowpack overall.

To the validation area are associated only in situ snow stratigraphies, already presented by Engeset at al. (2018). These measurements were acquired during the winter season 2024–2025 in dry snow conditions. A total of 27 observations, corresponding to approximately 12 % of the calibration dataset, were used.

3 Methods

3.1 Snowpack modelling

Snow observations directly measured by the AWSs were integrated with data derived by snowpack simulations. For this purpose, the SNOWPACK software was used (Bartelt and Lehning, 2002), with the operational setting employed for avalanche forecasting purpose in Livigno. The simulations were performed for a flat terrain (no preferential exposition), where the model was forced to follow the snowpack height measured by the AWSs, thus also simulating wind-driven snow erosion. The simulated data had an hourly temporal resolution. For each date and time of the available SAR acquisitions, we extracted the following snowpack variables (Xsv):

- snow height directly measured by the AWSs (HS);
- snow surface temperature directly measured by the AWSs (Tss);
- simulated snow water equivalent (SWE);
- average simulated snow density of the entire snowpack (ρHS);
- average simulated grain size of the entire snowpack (GS);
- average simulated liquid water content of the entire snowpack (LWC);
- height of the new snow of the last 24 hours ($HN24$).

3.2 SAR data processing

We used the open-source software SNAP for the entire standard preprocessing workflow of the Sentinel-1 GRD products, as well as for extracting the LIA. Initially, we applied the orbit state vectors provided by the satellite facility and then we performed radiometric calibration following the beta-nought (β^0) convention. Next, we removed the radiometric variability associated with topography using the Radiometric Terrain Correction algorithm proposed by Small (2011), obtaining the backscatter coefficient gamma-nought (γ^0). This coefficient was subsequently subjected to geometric terrain correction and speckle filtering using the Lee filter with a 9×9 pixels window size and 2 looks (Yommy et al., 2015). The images were finally resampled to a 10 m resolution.

For each preprocessed scene we computed the simplified $DpRVI_c$ index as proposed by Feng et al. (2024):

$$DpRVI_c = \frac{(\gamma^0_{\mathrm{VH}})^2 + 3\gamma^0_{\mathrm{VH}}\gamma^0_{\mathrm{VV}}}{(\gamma^0_{\mathrm{VH}} + \gamma^0_{\mathrm{VV}})^2}, \qquad (1)$$

where γ^0_{VH} represents the backscatter coefficient γ^0 in cross-polarization, while γ^0_{VV} represents the backscatter coefficient γ^0 in co-polarization. Both of them are measured in linear scale. Notice that, for a fixed value of γ^0_{VH}, the $DpRVI_c$ index decreases as γ^0_{VV} increases. Using data from the AWSs and Sentinel-2 optical imagery, we selected and averaged snow-free summer images to obtain a summer reference image ($DpRVI_c^{sr}$) for each of the two AGs. We then computed a new (adimensional) snow index, named Snow Index SAR ($SIsar$), as follows:

$$SIsar = DpRVI_c(t) - DpRVI_c^{sr}, \qquad (2)$$

where t represents the acquisition time over the snow season.

To analyze the relationship between the $SIsar$ index and each of the $Xsvs$, we extracted $SIsar$-time-series for the two regression sampling areas and the two satellite orbits. Wet snow presence in each scene was identified using γ^0 images, following the algorithm proposed by Nagler at al. (2016), and dates with wet snow conditions were neglected from the study. The Nagler's method was performed using reference images from the same acquisition dates as those used for $DpRVI_c^{sr}$ computation. The $SIsar$ values in the time series were computed by averaging the values within the regression sampling areas for the two different AGs, first making sure that data followed a normal distribution. Rarely, there were pixels with negative $SIsar$ values along the snow season, and these were excluded. For analyzing the dependence between our index and the LIA, we grouped and averaged the $SIsar$ values for LIA classes of 2° within the two LIA sampling areas. This last analysis was conducted under snow-free conditions as well as on several dates during the snow season. In this case, the pixels with negative $SIsar$ values were not excluded (the reason of this different choice will be clear later).

3.3 Mathematical modelling

Based on the theoretical background, the $SIsar$ index was assumed to be a function of the snowpack properties. Therefore, it could be expressed as:

$$SIsar = SIsar(HS, \rho HS, Tss, GS, LWC...). \qquad (3)$$

Our objective was to identify the most important snowpack variable Xsv, to approximate the $SIsar$

index as

$$SIsar \simeq f(Xsv), \tag{4}$$

where f was a suitable unknown function to be derived. Moreover, we then studied the dependence of the $SIsar$ index on the LIA in order to refine Eq. (4), namely we would like to write:

$$SIsar \simeq \tilde{f}(Xsv, LIA), \tag{5}$$

where, again, $\tilde{f}$ had to be derived. Finally, since the LIA is always known, by inverting Eq. (5) we would be able to compute an approximation Xsv_{mdl} for the variable Xsv.

To this end, we initially implemented a random forest algorithm to assess the importance of the snowpack variables in predicting the values of the $SIsar$ index sampled within the two regression sampling areas. The RF was performed using the R programming environment, running the algorithm proposed by Breiman (2001). This approach allows for the estimation of the importance of independent variables in predicting the dependent variable. Variable importance is assessed using the permutation method, which involves randomizing the values of each variable one at a time and evaluating the resulting decrease in model performances. It is worth noticing that the SWE variable was excluded from the RF model as it is dependent on other variables, indeed $SWE = HS \cdot (\rho HS/\rho_w)$, where ρ_w denotes the water density. The purpose of this analysis was purely qualitative, and the results were then validated through a statistical analysis. This latter analysis was conducted for the individual time series derived from the two regression sampling areas and the two separate AGs, as well as for all the data treated together. Specifically, Spearman's correlation coefficient (SCC) and Pearson's correlation coefficient (PCC) were calculated, and their significance was verified through the associated p-value obtained from a Z-test and a t-test, respectively. The SCC was used to assess the presence and the nature (positive or negative) of the correlation between the $SIsar$ index and the target Xsv. The SCC is a non-parametric measure, meaning it does not assume any specific distribution of the data, and it helps to identify monotonic relationships, whether linear or non-linear. In contrast, the PCC was used to determine whether the relationship between the $SIsar$ index and the chosen Xsv was linear or not. The PCC measures the strength and direction of a linear relationship between the data, and the assumption that those data are normally distributed must be made to verify the significance of the test (Hauke and Kossowski, 2011). For the variables that showed a significant linear correlation, we then fitted a linear regression model.

At this stage of the analysis, we selected the Xsv which showed the best linear correlation with the $SIsar$ index, and for which we could assume the theoretical property that $SIsar \simeq 0$ corresponds to snow-free conditions. Thus, we expressed the following relation:

$$SIsar \simeq f(Xsv) = a \cdot Xsv, \tag{6}$$

where $a > 0$ was derived with the least squares method. Therefore, the initial (linear) model for Xsv was given by

$$Xsv_{mdl\_lin} = \frac{SIsar}{a}. \tag{7}$$

Concerning the study of the dependence of the $SIsar$ index on the LIA, we expressed this relationship as:

$$SIsar \simeq \tilde{f}(Xsv, LIA) = g(LIA) \cdot Xsv, \tag{8}$$

where the function g was derived again with the least squares method and its shape was chosen according to the distribution of the data deriving from the LIA sampling areas. Indeed, when selecting a time and a LIA sampling area, we could assume (especially at the beginning of the winter season, when wind redistribution and variations in melting or metamorphism are not very influential) that Xsv remained constant in that zone. On the other hand, the LIA took on many different values. For this reason, the function g could be approximated as $g(LIA) \simeq SIsar/Xsv$, which should be independent on Xsv. Therefore, the final model for Xsv was:

$$Xsv_{mdl\_LIA} = \frac{SIsar}{g(LIA)}. \tag{9}$$

3.4 Model validation strategy

The validation of our model for approximating Xsv was divided into three parts. Initially, we compared, in terms of root mean squared error (RMSE) and mean absolute error (MAE), the approximations for Xsv given by Eqs. (7) and (9), using as reference the measurements of the two AWSs (Xsv_{msr}) inside the model calibration area. Note that we excluded from this analysis all pixels that exhibited negative values of the $SIsar$ index during the snow accumulation season, which were very limited in number. Secondly, we performed a mathematical analysis to establish the validity of the LIA dependency through the function g. When we initially derived the value a we considered values of the $SIsar$ index related to different $LIAs$. For this reason, the weighted average value $\bar{g}$ of the function g should be similar to a. Note that we had to consider a weighted average because some $LIAs$ were more recurring than others. Recall that the regression sampling areas and the LIA sampling areas were independent of each other. Finally, using

Eq. (9), we computed the values of Xsv_{mdl_LIA} for the Norwegian validation sampling area during the months of December 2024 and January 2025. To demonstrate the model's applicability in a location significantly different from the one it was calibrated on, we compared Xsv_{mdl_LIA} with field measurements conducted in the validation sampling area.

4 Results

4.1 SIsar index and snowpack variables

Due to the limited dataset available, the results of the random forest analysis are exploratory. The importance values of the variables are uniformly low and, therefore, not reported, as they are likely affected by the small sample size and should not be overinterpreted. Nevertheless, the random forest model suggests that the variable $HN24$ is not important for predicting the $SIsar$ index, while HS emerged as the most important predictor, followed by ρHS, GS, LWC, and Tss. The results of the statistical analysis, conducted on the entire dataset (which includes all regression sampling areas and acquisition geometries), are presented in Table 1. The analysis reveals significant correlations between the $SIsar$ index and several variables, including HS, SWE, ρHS, and GS. Specifically, there is a moderate-to-strong positive relationship with both HS and SWE, a moderate positive correlation with ρHS, and a moderate-to-low negative correlation with GS. These findings align with the results from the random forest model. The PCCs and the related p-value tests indicate that the linear relationships between the $SIsar$ index and both HS and SWE are strong, while no robust linear relationship is found between the $SIsar$ index and ρHS. Moreover, the p-values associated to the linear regression model show that, for both HS and SWE, the regression slope is significant. However, only for HS the intercept is not significant. Therefore, only for HS, we can set the intercept to zero, implying that snow-free conditions should correspond to a value of $SIsar \simeq 0$ (see Section *3.3*). This, together with the fact that the best PCC corresponds to HS, supports the selection of this variable as the candidate Xsv for the model. Therefore, hereafter we set $Xsv = HS$. In particular, the quality of the linear regression with intercept set equal to zero is almost the same as the one obtained for a generic intercept, indeed the R^2 coefficients are 0.493 and 0.495 respectively. The coefficient a of the linear relationship between HS and the $SIsar$ index (see Eq. (6)) is approximately $6.00 \cdot 10^{-4}$ cm^{-1}, as reported in Figure 5(a). The results of the statistical analysis conducted for each individual regression sampling area are not presented in tabular form for brevity. However, the findings are consistent with those reported for the analysis conducted on the entire dataset. Focusing only on the most influential variables, a strong positive PCC with the $SIsar$ index is observed for HS and SWE across all areas and AGs. In particular, the highest PCC values for HS and SWE are at Vall for AG 15, with PCC equal to 0.802 and 0.800, respectively. Additionally, the correlation intensity order among the variables is in line with the results from the analysis of the entire dataset, except for the Gessi area in AG 168, where SWE shows a slightly better linear correlation with the $SIsar$ index than HS (PCC equal to 0.761 against 0.756). Finally, the best correlations are in general related to the AG 15 (afternoon).

4.2 SIsar index and local incidence angle

Figure 2 shows examples of the behavior of the $SIsar$ index for 2° LIA classes across the different LIA sampling areas, at different times during the snow season, and under snow-free conditions. In both areas, for all acquisitions with snow-free conditions, the $SIsar$ index on average remains approximately constant as the LIA increases, with values close to zero. When analyzing the relationship in both LIA sampling areas for all dates with snow cover, we first observe that the $SIsar$ index shows negative values for angles approximately lower than 30°, even if HS is not zero. For all these acquisitions, for angles greater than approximately 30°, the relationship between the $SIsar$ index and the LIA follows a parabolic shape, which suggests a relationship between them in the presence of snow.

As one can notice from Figure 3, the point where the curves showing the relation between the LIA and the $SIsar$ index intersect the x-axis is consistently around $25° - 30°$, and again we see that the relationship between the $SIsar$ index and the LIA follows a parabolic shape for larger angles. In particular, as HS increases the parabolic shape expands vertically upwards. This suggests that the $SIsar$ index can be expressed as Eq. (8). Clearly, the function g is determined from the set of parabolic functions and using the least-squares method.

From the least squares method, we obtain the following equation for $g(LIA)$, as represented in Figure 4:

$$g(LIA) = a_0 + a_1 \cdot LIA + a_2 \cdot LIA^2, \qquad (10)$$

where the LIA is expressed in degrees, $a_0 = 4.41 \cdot 10^{-3}$ cm^{-1}, $a_1 = 2.04 \cdot 10^{-4}\ {}^{\circ -1} \cdot$ cm^{-1}, and $a_2 = -1.80 \cdot 10^{-6}\ {}^{\circ -2} \cdot$ cm^{-1}. The zeros of $g(LIA)$ are approximately 29.1° and 84.4°. Since we observe that for LIA values below approximately 30° the $SIsar$ index is always negative, even when HS is nonzero, we exclude all areas with $LIA < 30°$ in the

Snowpack variable (Xsv)	**SCC**	**SCC p − value**	**PCC**	**PCC p − value**	**Linear regression intercept p − value**	**Linear regression slope p − value**
HS	0.552	$2.60 \cdot 10^{-9}$	0.704	$3.23 \cdot 10^{-16}$	0.485	$3.23 \cdot 10^{-16}$
SWE	0.553	$2.43 \cdot 10^{-9}$	0.700	$5.11 \cdot 10^{-16}$	0.00761	$5.11 \cdot 10^{-16}$
ρHS	0.438	$6.43 \cdot 10^{-9}$	0.492	$2.07 \cdot 10^{-7}$	-	-
GS	-0.295	0.00302	-0.275	0.00566	-	-
Tss	0.0367	0.717	0.0682	0.500	-	-
$HN24$	0.199	0.0471	0.155	0.124	-	-
LWC	0.349	$3.72 \cdot 10^{-4}$	0.139	0.168	-	-

Table 1: Summary of the results of the statistical analysis for each snowpack variable Xsv. The linear regression model is performed only for those variables showing a significant and high PCC.

implementation of the model. Areas with $LIA > 80°$ are also removed because they are more prone to SAR shadowing errors. Due to these choices, we obtained rarely negative $SIsar$ values when we modelled HS during the snow accumulation season (see Sections *3.2* and *3.4*). In particular, Eq. (9) is well-defined since $g(LIA) \neq 0$ for all $LIAs$ of interest.

4.3 Models comparison and validation

When applied to the calibration area, the model for HS given by Eq. (7) leads to a RMSE equal to 57.2 cm and a MAE equal to 46.0 cm. With the LIA correction, the errors drop significantly, indeed using Eq. (9) the RMSE becomes 34.6 cm while MAE 28.3 cm. These values represent a 39.5 % decrease RMSE and a 38.5 % decrease in MAE. Plotting HS_{mdl_LIA} against HS_{msr} (Figure 5(b)), we observe that $HS_{mdl\_LIA} \simeq c_1 \cdot HS_{msr}$, with $c_1 = 0.841$. It is important to note that a perfect model would lead to a value of c_1 equal to 1. To mathematically verify the validity of $g(LIA)$ we compute its weighted average $\bar{g}$ as explained in Section *3.4*, obtaining $\bar{g} = 9.70 \cdot 10^{-4}$ cm^{-1}, which is of the same order of magnitude as the coefficient $a = 6.00 \cdot 10^{-4}$ cm^{-1} of Eq. (7). It is worth noticing that the approximation $a \simeq \bar{g}$ becomes better if we consider $c_1 \cdot \bar{g} = 8.16 \cdot 10^{-4}$ cm^{-1} instead of $\bar{g}$. Finally, using Eq. (9) to estimate HS in the validation area around Tromsø(the validation dataset; see Figure 6) we obtain that $HS_{mdl\_LIA} \simeq c_2 \cdot HS_{msr}$, with $c_2 = 0.923$. The RMSE is 30.7 cm while the MAE is 24.3 cm. See Table 2 for a comparison of the errors.

HS estimation	**RMSE**	**MAE**
HS_{mdl_lin} (Livigno)	57.2 cm	46.0 cm
HS_{mdl_LIA} (Livigno)	34.6 cm	28.3 cm
HS_{mdl_LIA} (Tromsø)	30.7 cm	24.3 cm

Table 2: Errors related to the different models and datasets.

5 Discussion

5.1 Correlations of the SIsar index with snowpack variables

The statistical analysis indicated that the $SIsar$ index, and consequently SAR signal depolarization within the snowpack, is a complex function of several snowpack parameters. Nevertheless, since SAR measurements are of great interest, especially in poorly monitored areas where no additional observations are generally available, we aimed to limit the dependency to just one of the most significantly linearly correlated variables. These are HS and SWE, in accordance with several other studies (Lievens et al., 2019; Patil et al., 2020; Snehmani et al., 2015). The selection of HS as candidate Xsv is supported by the fact that it is the only snowpack variable for which the intercept value is not statistically significant, thereby fulfilling the theoretical condition that $SIsar \simeq 0$ corresponds (on average) to a snow-free state. The Spearman's correlation coefficient suggests that the $SIsar$ index, and thus signal depolarization, increases also with ρHS. One possible explanation for this increase is that thicker and denser snowpacks contain a larger snow mass, more grains, and more potential discontinuities in the snowpack dielectric constant. Consequently, there will be more opportunities for signal depolarization, as reported in Lievens et al. (2019). Another possible explanation arises from the results presented by Paloscia et al. (2017), where a negative relationship between the backscatter coefficient σ^0 in HH polarization (σ^0_{HH}) from Cosmo-SkyMed

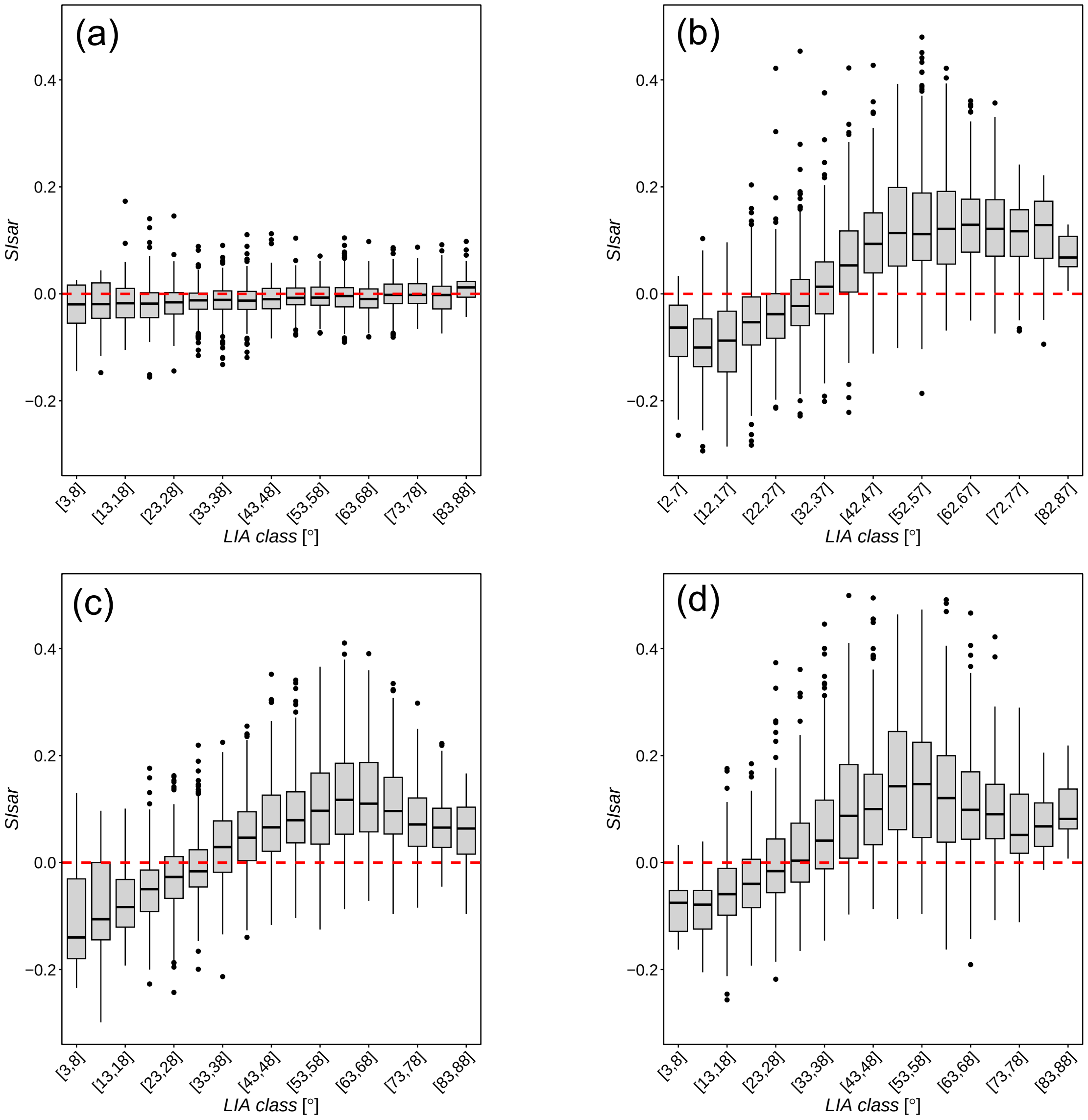

Figure 2: Box plots of 2° LIA classes vs. $SIsar$ index values over the course of the snow accumulation season (i.e., for increasing values of HS measured by the AWSs within the LIA sampling areas). (a) Gessi AG 15, 08.08.2023, snow-free conditions. (b) Gessi AG 168, 23.11.2023, $HS_{msr} = 60$ cm. (c) Gessi AG 15, 24.11.2023, $HS_{msr} = 60$ cm. (d) Vall AG 168, 29.12.2023, $HS_{msr} = 100$ cm.

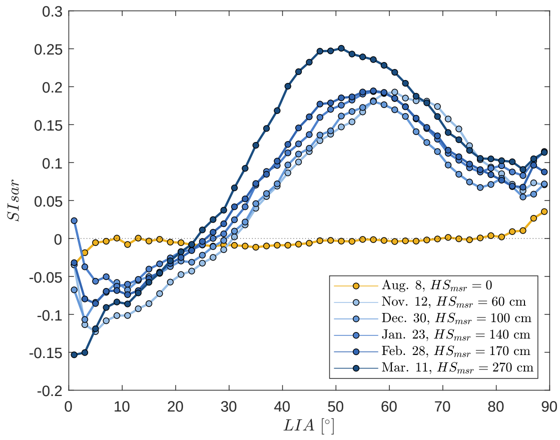

Figure 3: Mean $SIsar$ values, sampled from the LIA sampling areas, grouped into LIA classes of 2° width. The blue color scale represents the increasing average HS values measured by the two AWSs for different acquisition dates along the 2023-2024 season. Yellow points represent the values from an acquisition date in summer 2023.

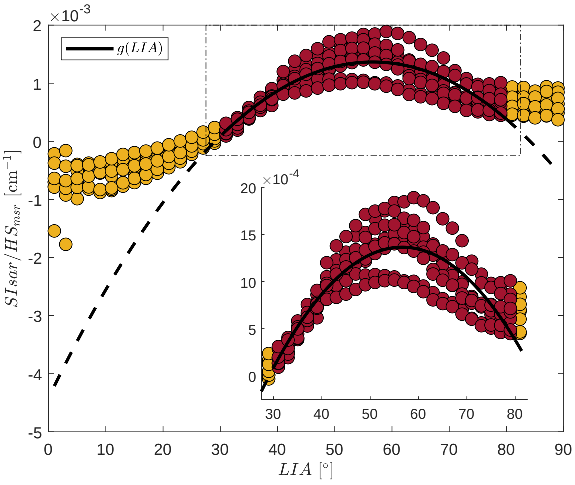

Figure 4: Mean $SIsar$ values normalized by HS measured by the AWSs grouped into LIA classes of 2° width. Data derive from the beginning of the season, when we could assume that HS was representative of the entire LIA sampling areas. Values for $LIA < 30°$ and $LIA > 80°$ are reported in yellow, while values between 30° and 80° in red. In black we report the function $g(LIA)$, inferred on the data.

X-band platform and snow density was observed (σ^0 is obtained from β^0 but, unlike γ^0, without the radiometric terrain correction; Small (2011)). Since the $SIsar$ index is based on the variations of the $DpRVI_c$ index, which decreases as γ^0_{VV} increases, an increase of our index is expected if co-polarized backscatter decreases with snow density (indeed, we expect γ^0_{VV} to decrease/increase as σ^0_{HH} decreases/increases since they are both related to co-polarization). However, the Pearson's correlation coefficient suggests that the relation between the $SIsar$ index and ρHS is not linear. This is in line with the linear relationship resulted between the $SIsar$ index and the SWE: if both ρHS and HS would be linearly correlated with the index, then the SWE would be quadratically correlated with it (this directly follows from the definition of SWE; see Section *3.3*). Concerning the fact that the intercept can be set equal to zero for HS but not for the SWE, this is probably a consequence of the fact that the SWE is not well-defined in absence of snow: as snow fades away, both its mass and volume tend to zero, implying that ρHS cannot be defined in absence of snow. Furthermore, Paloscia et al. (2017) observed that the co-polarized band of Cosmo-SkyMed σ^0_{HH} increases with larger GS, which could similarly explain the slight decrease in the $SIsar$ index that we observe for increasing GS for the reasons previously described. However, further specific analyses are necessary to better understand these complex behaviors. The results do not show a significant correlation between the $SIsar$ index and Tss. However, Baumgartner at al. (1999) demonstrated that SAR backscatter is sensitive to variations in near-surface snow temperature. The statistical analysis conducted for individual regression sampling areas and individual acquisition geometry confirm the one conducted on the entire dataset. The evidence that the Pearson's correlation coefficients for individual stations and acquisition geometry slightly differ from the one obtained when considering all data together suggests that variations in morphology, land cover, and local climatic conditions lead to slight differences in the relationship between the $SIsar$ index and any Xsv. Consequently, a local fitting approach should perform slightly better than a global one. These results are consistent with the findings of Jans et al. (2025).

5.2 Influence of the local incidence angle on the SIsar index

The analysis of the relationship between the $SIsar$ index and the LIA under snow-free and snow-covered conditions was revealing. No significant dependence on the LIA is observed for any of the snow-free acquisitions in either analysis area, with

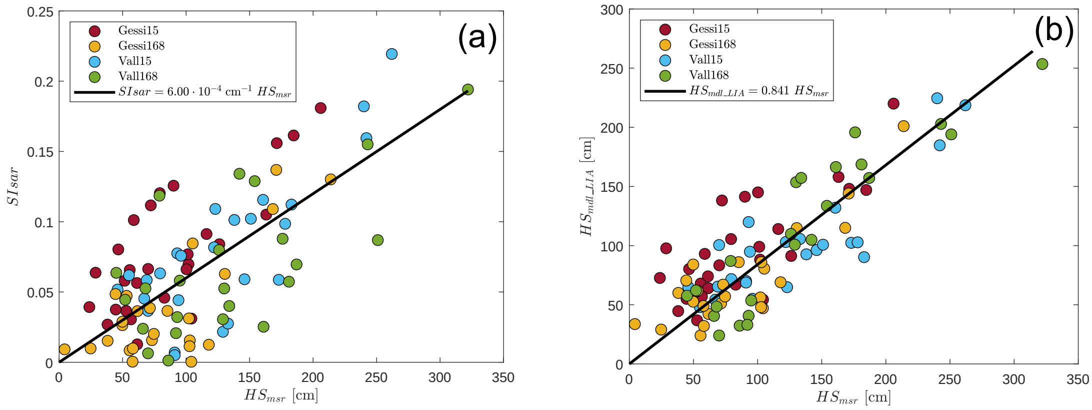

Figure 5: Scatter plot of HS_{msr} vs. $SIsar$. (b) Scatter plot of HS_{msr} vs. HS_{mdl_LIA}. The linear regressions computed with the least square method are also represented.

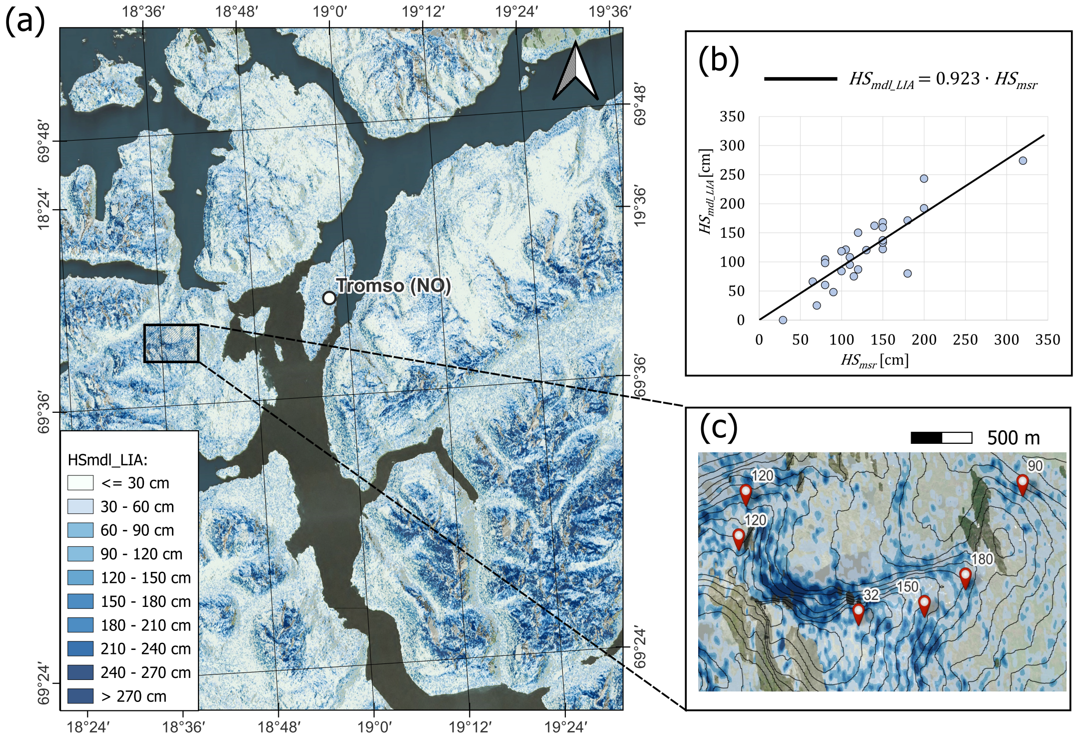

Figure 6: Snow depth estimation for the validation area. (a) Overview of HS_{mdl_LIA} between 31.12.2024 and 01.01.2025. (b) HS_{msr} vs. HS_{mdl_LIA}. (c) Particular of (a) showing in situ observations carried out between 30.12.2024 and 02.01.2025 (no significant variation of HS occurred in this time window).

values on average around zero. On the other hand, in all acquisitions under snow-cover conditions, we first observe that $SIsar$ values are negative for low incidence angles, specifically for LIA values below approximately $25° - 30°$. For incidence angles greater than 20°, the relationship between our index and the LIA takes on a parabolic shape, increasing up to around 55° before decreasing again. This suggest that $DpRVI_c$ variations in presence of snow above the ground are significantly influenced by the LIA, and that the latter must be taken into account for dual-polarimetric SAR retrieval of HS (despite the SAR products were radiometrically terrain corrected for the LIA within the preprocessing phase). A complex relationship between SAR backscatter coefficients and derived vegetation indices has been already demonstrated in the presence of vegetation cover above the ground by Kaplan et al. (2021). Since the behavior of a vegetation volume can be linked to the presence of snow over bare soil, we believe our observations are valid. Since the $SIsar$ index is consistently negative during the accumulation season for LIA values lower than 30°, snow cover monitoring is not possible in this situation. The negative values of the $SIsar$ index for low $LIAs$ are consistent with the findings of Jans et al. (2025), which highlighted that the Sentinel-1 co-polarized backscatter coefficient (σ^0_{VV}) increases with HS only for small incidence angles. Since the $DpRVI_c$ index decreases as γ^0_{VV} increases, it is expected to be lower for low LIA values when HS increases, leading to negative $SIsar$ values. Another possible explanation, in line with the work of Keskinen at al. (2022) on avalanche deposit detection rates, is that for small $LIAs$, the specular backscatter produced by the soil is redirected towards the sensors, leading to higher backscatter values, particularly in VV polarization (more sensitive to surface backscatter than VH polarization). For LIA values between approximately 30° and 50°, the increase in $SIsar$ with the LIA for a constant HS can be explained by the fact that as the LIA increases, a larger volume of snow is traversed by the SAR signal, leading to more opportunities for signal depolarization and different interactions with layered structures. This tends to increase the backscatter coefficient γ^0_{VH}. Furthermore, in accordance with the work of Keskinen at al. (2022), for these LIA values, the specular backscatter produced by the soil beneath the snowpack is directed away from the sensor, while the influence of the rough snow surface becomes less negligible. This leads to a greater decrease in γ^0_{VV} than γ^0_{VH}. The decrease of the $SIsar$ values for high $LIAs$ is more difficult to interpret. Some possible explanations include a combination of factors such as the dominant specular scattering mechanism, many pixels being in shadow areas, and travel path of the signal trough the snowpack being so long that its energy absorption is no longer negligible, even at C-band (Rott et al., 2021). However, further specific studies are needed to confirm or refute these hypotheses. See Figure 7 for a schematic representation of the influence of the LIA on the $DpVRI_c$ index-variations. All these considerations, together with the fact that the parabolic curve describing the dependence of the $SIsar$ index on the LIA extends upwards as the accumulation season progresses (i.e., as HS increases), support the choice of Eq. (8), and hence also the estimation for HS given by Eq. (9). Finally, the similar behaviors of the $SIsar$ index normalized by the measured HS observed in both LIA sampling areas at different times of the snow season suggests that $g(LIA)$ is not significantly dependent on local or temporal conditions. Notice that acquisitions refer to two very different seasons in terms of structure and physical properties of the snowpack.

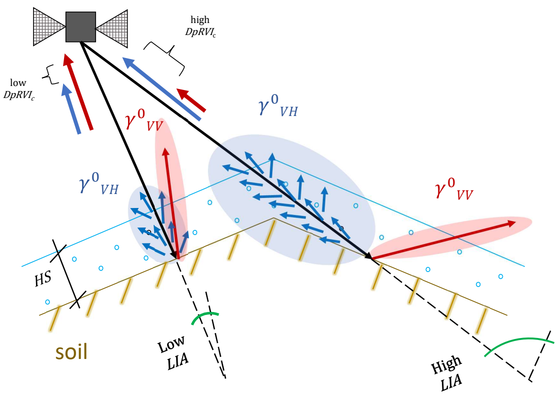

Figure 7: Schematic representation of the influence of the local incidence angle on the $DpRVI_c$ index-variations.

5.3 *Effectiveness of considering the local incidence angle within the model*

When we approximated HS trough Eq. (9) (i.e., HS_{mdl_LIA}) we obtained a significant improvement with respect to the usage of Eq. (7) (i.e., HS_{mdl_lin}), both in terms of root mean square error and mean absolute error. Furthermore, the values of the weighted average $\bar{g}$ of the function $g(LIA)$ is of the same order of magnitude of the slope coefficient a of the linear regression. Differences between the values of $\bar{g}$ and a are attributed to the several sources of errors: we considered only the most influential snowpack variable, variations in soil properties that we did not consider could affect the values of the $SIsar$ index, and the datasets used to derived a and $g(LIA)$ are different and independent of each other. This also explains why

$HS_{mdl\_LIA} \simeq c_1 \cdot HS_{mrd}$ with c_1 not exactly equal to 1: the slope c_1 incorporates the errors deriving from the factors just described. However, the results obtained not only confirm the significance of the relationship between the $SIsar$ index and the LIA, but also indicate that correcting the index with a function accounting for its dependence on the LIA leads to a substantial improvement. Therefore, the LIA has a non-negligible influence on SAR signal depolarization when snow is present above the ground.

The results of the validation performed with the in situ measurements carried out in Tromsø, Norway, further support the correctness of the modelling. The relation $HS_{mdl\_LIA} \simeq HS_{mrd}$ was successfully verified, and both the RMSE and the MAE are similar to the values obtained for Livigno, Italy. This suggests a global applicability of the model, even if a local calibration with in situ observations is recommended, as already discussed in Section *5.1*. As shown in Figure 6, mapping HS_{mdl_LIA} for the model validation area reveals a high degree of heterogeneity in snow cover distribution. At a large-scale, we observe that zones with greater snow accumulation are generally found at higher elevations (see Figure 6(a)). Conversely, at a small-scale, we observe that the snow distribution appears highly irregular, with eroded peaks and ridges, while significant deposits are found in bowls and gullies (see Figure 6(c)). This latter observation aligns with both field measurements available for the period under analysis, and the regional climate, which is characterized by frequent wind transport events. It is important to note that, within the same acquisition, we used field observations that were proximal to one another (with a minimum spacing of approximately 100 m) and were located on different slopes and aspects (i.e., corresponding to different $LIAs$). This implies that, although the obtained MAE was slightly higher than the one obtained in the work of Lievens et al. (2022), where HS was mapped for a 500 m resolution, or in the one of Feng et al. (2024), the proposed model demonstrates a good ability in describing snow depth variations at the small-scale (i.e., within the same slope). This is particularly relevant for avalanche forecasting purposes, since avalanche forecasters are interested in detecting the complex snow cover heterogeneity of the alpine environment, which is influenced by wind transport, avalanches, and the various metamorphic processes occurring at different aspects (Plattner et al., 2004).

5.4 Model limitations

As reported in Appendix **A**, we observe that our model significantly overestimates HS when wet snow layers are embedded within dry snow layers. This configuration is typical during the early or late stages of the snow season, particularly when dry snowfall accumulates over an existing wet snow surface due to a decrease in frost level during a precipitation event (Colbeck, 1982). This overestimation can be theoretically interpreted as follows: both γ^0_{VV} and γ^0_{VH} should drop in presence of wet snow since the signal is absorbed and hence unable to penetrate further in depth. However, the presence of dry snow on the surface results in a γ^0_{VH} increase, which is more sensitive to volumetric backscatter than γ^0_{VV}. This implies a significant increase of the $DpRVI_c$ index since it increases as the difference between co- and cross- polarization backscatter decreases. Under these conditions, the method of Nagler at al. (2016) used for SAR-based wet snow retrieval may fail since it relies on both VV and VH bands. Notably, in these conditions, the average liquid water content (LWC) of the snowpack is not particularly high, considering that an LWC threshold of 1 % is commonly used to distinguish dry from wet snow (Mitterer at al., 2013).

The variations of HS_{mdl_LIA} in bare-soil conditions reflect the dependence of $DpRVI_c$ by external factors, such as soil moisture, ground surface temperature, and variations in low-lying vegetation (Das and Pandey, 2024). This confirms that the method is inherently unable to clearly discriminate between the presence and absence of snow, as noted in Jans et al. (2025). Indeed, $SIsar \simeq 0$ in snow-free conditions (see Section *3.3*) is verified only on average, not for the single acquisition.

Finally, even if further studies are needed to confirm this behavior, the elevate number of pixels with negative $SIsar$ values at the beginning of the snow season confirms what reported in Lemos and Rihelä (2024), who demonstrates the difficulties of Sentinel-1 based HS retrieval in very thin snowpacks.

6 Conclusions and future work

In this study, we presented a novel mathematical model that enhances small-scale snow depth monitoring leveraging dual-polarimetric Sentinel-1 SAR data. Specifically, we introduced a new index, named Snow Index SAR ($SIsar$), which is defined as the difference between the Dual Polarimetric Radar Vegetation Index ($DpRVI_c$) computed under snow-covered conditions and average snow-free conditions. The model was calibrated using two independent datasets from the Livigno area (Italy, Central Italian Alps), which include data collected from two proximal automatic weather stations and simulated with the SNOWPACK snow cover model. These datasets span two winter seasons and cover two different acquisition geometries.

A statistical analysis revealed that the $SIsar$ index is influenced by several snowpack variables. In particular, it shows a linear correlation with the snowpack height and the snow water equivalent, while statistically significant relationships were also found with the average snowpack density and grain size. The $SIsar$ index generally increases with these quantities, except for the average grain size, where a low negative correlation was observed. The strongest linear correlation is with the snowpack height, so we initially applied a linear regression model to estimate snow depth from $SIsar$ values. Notably, the model aligns well with theoretical expectations, confirming that $SIsar \simeq 0$ corresponds (on average) to snow-free conditions.

A key result of this study is the demonstration of the strong influence of the local incidence angle (LIA) on the $SIsar$ index in presence of snow, despite the SAR products are radiometrically terrain corrected for the LIA within the preprocessing phase. For angles below 30°, the $SIsar$ index is almost always negative, a behavior we explained theoretically. Between 30° and 80°, its relationship with the LIA follows a parabolic curve. The derivation of this curve allowed us to correct for the angular dependence of signal depolarization for increasing snowpack height. This correction significantly improved snowpack height estimations compared to the initial linear model, reducing the mean absolute error (MAE) by 38.5 % and the root mean square error (RMSE) by 39.5 %.

The final model was verified and validated using a third independent dataset from Tromsø, Norway, which differs significantly from Livigno in terms of snow and weather conditions. The validation results showed a RMSE of 30.7 cm and a MAE of 24.3 cm, providing preliminary evidence of the model's potential for global applicability. Finally, an additional analysis identified the summer $DpRVI_c$ variations and the presence of wet snow layers inside the snowpack as significant sources of error.

Since the model was calibrated with snowpacks not deeper than 300 cm, its validity for thicker snow accumulations remains untested. Future studies will address these gaps, particularly focusing on $DpRVI_c$ variations in snow-free conditions and explore potential model adjustments for deeper snowpacks, also considering that, theoretically, the signal absorption by Sentinel-1 may become non-negligible for very thick snow layers. Moreover, our study focused on alpine terrain, suggesting that the quality of snowpack height estimations under different terrains and soil covers should be assessed.

A Wet snow and summer *SIsar* index-variations

To further investigate the model results, we compared the evolution of the measured snowpack height (i.e., HS_{msr}) with the modelled one (i.e., HS_{mdl_LIA}) on the two regression sampling areas and across two seasons (2022/23 and 2023/24). As illustrated in Figure A1 for Gessi with AG 15, the HS_{mdl_LIA} exhibits larger fluctuations compared to HS_{msr}. Notice that our model significantly overestimates HS when wet snow layers are present beneath dry snow layers.

Moreover, we assessed the model's capability to distinguish between snow-free and snow-covered conditions. However, pixels with negative $SIsar$ values were very common during the summer period, hence removing all of them was not possible (see Section *3.2*). In Figure A1 are shown the average values of HS_{mdl_LIA} during the summer 2023 computed for the Gessi regression sampling area and without removing the pixels with a negative value of the $SIsar$ index. During the observed summer period, the RMSE was 30.5 cm and the MAE was 25.6 cm, which are consistent with the model's performances obtained for the snow-covered seasons. However, due to the HS modelled fluctuations, it was not possible to detect snow-free conditions with our model. Anyway, on average $HS_{mdl\_LIA} \simeq 0$, which is in line with the results presented in Section *4.2*.

Finally, we noticed an increase in the number of pixels showing negative $SIsar$ values under snow-covered conditions at the beginning of the season, when the snowpack is generally thin.

Data availability. The in situ snow stratigraphies of the Norwegian model validation area are freely available at `https://regobs.no/?SelectedNumberOfDays=3&&NWLat=72.47527631092942&NWLon=-21.621093750000004&SELat=55.178867663282006&SELon=89.384765625` (Varsom Regobs, 2018). The data measured by the Vall AWS are available at `https://www.arpalombardia.it/temi-ambientali/meteo-e-clima/form-richiesta-dati/` (ARPA Lombardia, 2025). The data measured by the Gessi AWS and the snow stratigraphies of the Italian model calibration area are available from the corresponding author.

Author contributions. AM: Conceptualization, Investigation, Formal analysis, Methodology, Validation, Visualization, Writing - original draft. JB: Formal analysis, Methodology, Validation, Visualization, Writing - original draft. FL: Supervision, Writing - review and editing. GV: Data curation. MM: Data curation. FM: Supervision.

Acknowledgments. AM acknowledges Alpsolut S.r.l. for fully funding his PhD. The work

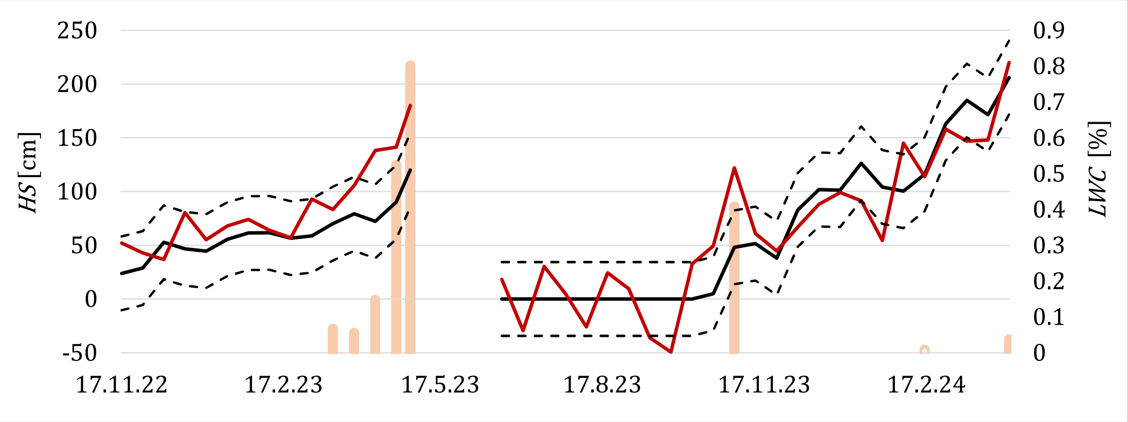

Figure A1: Comparison between HS_{mdl_LIA} (solid red line) and HS_{msr} (solid black line; Gessi AWS) during the two full seasons 2022/23 and 2023/24. The dotted black lines are obtained by shifting the solid one upward and downward by 31.0 cm, which is the RMSE obtained by estimating HS considering only the Gessi data. Pixels with negative $SIsar$ values were not removed during the summer period to compute HS_{mdl_LIA}. The bar chart represents the liquid water content (LWC).

of JB was performed in the frame of activities sponsored by the University of Parma and by the Italian National Group of Mathematical Physics (GNFM-INdAM). JB also thanks the support of the project PRIN 2022 PNRR "Mathematical Modelling for a Sustainable Circular Economy in Ecosystems" (project code P2022PSMT7, CUP D53D23018960001) funded by the European Union - NextGenerationEU, PNRR-M4C2-I 1.1, and by MUR-Italian Ministry of Universities and Research.

References

ARPA Lombardia, 2025. Vall dataset. `https://www.arpalombardia.it/temi-ambientali/meteo-e-clima/form-richiesta-dati/` (accessed 1.13.25).

Awasthi, S., Varade, D., 2021. Recent advances in the remote sensing of alpine snow: a review. GIsci. Remote Sens., 58, 852—888. `https://doi.org/10.1080/15481603.2021.1946938`.

Barnett, T.P., Adam, J.C., Lettenmaier, D.P., 2005. Potential impacts of a warming climate on water availability in snow-dominated regions. Nature, 438, 303—309. `https://doi.org/10.1038/nature04141`.

Bartelt, P., Lehning, M., 2002. A physical SNOWPACK model for the Swiss avalanche warning: Part I: Numerical model. Cold Reg. Sci. Technol., 35, 123–145. `https://doi.org/10.1016/S0165-232X(02)00074-5`.

Baumgartner, F., Jezek, K., Forster, R.R., Gogineni, S.P., Zabel, I. H. H., 1999. Spectral and angular ground-based radar backscatter measurement of Greenland snow facies. IEEE Int. Geosci. Remote Sens. Symposium, 2, 1053-–1055. `https://doi.org/10.1109/igarss.1999.774530`.

Breiman, L., 2001. Random Forests. Mach. Learn., 45, 5-–32. `https://doi.org/10.1023/A:1010933404324`.

Chang, W., Tan, S., Lemmetyinen, J., Tsang, L., Xu, X., Yueh, S. H., 2014. Dense media radiative transfer applied to SnowScat and SnowSAR. IEEE J. Sel. Top. Appl. Earth Obs. Remote Sens., 7, 3811-–3825. `https://doi.org/10.1109/JSTARS.2014.2343519`.

Colbeck, S.C., 1982. An overview of seasonal snow metamorphism. Rev. Geophys., 20, 45-–61, `https://doi.org/10.1029/RG020i001p00045`.

Das, D., Pandey, A., 2024. Soil moisture retrieval from dual-polarized Sentinel-1 SAR data over agricultural regions using a water cloud model. Environ. Monit. Assess., 197, 52. `https://doi.org/10.1007/s10661-024-13510-4`.

Dramis, F., Guglielmin, M., 2001. Permafrost Investigations in the Italian Mountains: The State of the Art. Springer, NATO Sci. S., 76. `https://doi.org/10.1007/978-94-010-0684-2_17`.

EAWS, 2025. European Avalanche Warning Service. `https://www.avalanches.org/fatalities/` (accessed 1.13.25).

Engeset, R.V., Ekker, R., Humstad, T., LandrÃ, M., 2018. Varsom:regobs - a common real-time picture of the hazard situation shared by mobile information technology. Proceedings of the International Snow Science Workshop, Innsbruck, Austria, 1573–1577. `https://arc.lib.montana.edu/snow-science/item/2822`.

European Union, 2021. Copernicus Global Digital Elevation Model (GLO-30). `https://dataspace.copernicus.eu/explore-data/data-collections/copernicus-contributing-missions/collections-description/COP-DEM` (accessed 1.13.25).

Feng, T., Huang, C., Huang, G., Shao, D., Hao, X., 2024. Estimating snow depth based on dual polarimetric radar index from Sentinel-1 GRD data: A case study in the Scandinavian Mountains. Int. J. Appl. Earth Obs., 130, 103873. `https://doi.org/10.1016/j.jag.2024.103873`.

Hauke, J., Kossowski, T., 2011. Comparison of values of Pearson's and Spearman's correlation coefficients on the same sets of data. Quest. Geographicae, 30, 87–93. `https://doi.org/10.2478/v10117-011-0021-1`.

Jans, J.F., Beernaert, E., De Breuck, M., Brangers, I., Dunmire, D., De Lannoy, G., Lievens, H., 2025. Sensitivity of Sentinel-1 C-band SAR backscatter, polarimetry and interferometry to snow accumulation in the Alps. Remote Sens. Environ., 316, 114477. `https://doi.org/10.1016/j.rse.2024.114477`.

Kaplan, G., Fine, L., Lukyanov, V., Manivasagam, V.S., Tanny, J., Rozenstein, O., 2021. Normalizing the local incidence angle in sentinel-1 imagery to improve leaf area index, vegetation height, and crop coefficient estimations. Land, 10, 680. `https://doi.org/10.3390/land10070680`.

Kapper, K.L., Goelles, T., Muckenhuber, S., Trügler, A., Abermann, J., Schlager, B., Gaisberger, C., Eckerstorfer, M., Grahn, J., Malnes, E., Prokop, A., Schöner, W., 2023. Automated snow avalanche monitoring for Austria: State of the art and roadmap for future work. Front. Remote Sens., 4. `https://doi.org/10.3389/frsen.2023.1156519`.

Keskinen, Z., Hendrikx, J., Eckerstorfer, M., Birkeland, K., 2022. Satellite detection of snow avalanches using Sentinel-1 in a transitional snow climate. Cold Reg. Sci. Technol., 199, 103558. `https://doi.org/10.1016/j.coldregions.2022.103558`.

Lemos, A., Riihelä, A., 2024. Snow depth derived from Sentinel-1 compared to in-situ observations in northern Finland. EGUsphere [preprint], `https://doi.org/10.5194/egusphere-2024-869`.

Lievens, H., Demuzere, M., Marshall, H.P., Reichle, R.H., Brucker, L., Brangers, I., de Rosnay, P., Dumont, M., Girotto, M., Immerzeel, W. W., Jonas, T., Kim, E.J., Koch, I., Marty, C., Saloranta, T., Schöber, J., De Lannoy, G.J.M., 2019. Snow depth variability in the Northern Hemisphere mountains observed from space. Nat. Commun., 10, 4629. `https://doi.org/10.1038/s41467-019-12566-y`.

Lievens, H., Brangers, I., Marshall, H. P., Jonas, T., Olefs, M., De Lannoy, G., 2022. Sentinel-1 snow depth retrieval at sub-kilometer resolution over the European Alps. The Cryosphere, 16, 159—177. `https://doi.org/10.5194/tc-16-159-2022`.

Mandal, D., Kumar, V., Ratha, D., Dey, S., Bhattacharya, A., Lopez-Sanchez, J.M., McNairn, H., Rao, Y.S., 2020. Dual polarimetric radar vegetation index for crop growth monitoring using sentinel-1 SAR data. Remote Sens. Environ., 247, 111954. `https://doi.org/10.1016/j.rse.2020.111954`.

Mariani, A., Abrahamsen, A.B., Bridle, D., Ingeman-Nielsen, T., Cicoira, A., Monti, F., Marcer, M., 2023. Snowpack and avalanche characterization over the 2021–2022 winter season in Sisimiut, West Greenland. Front. Earth. Sci., 11, 1134728. `https://doi.org/10.3389/feart.2023.1134728`.

McClung, D., Schaerer, P. A., 2023. The avalanche handbook, fourth ed., The Mountaineers Books, Seattle, USA. `https://www.mountaineers.org/books/books/the-avalanche-handbook-4th-edition`.

Mitterer, C., Techel, F., Fierz, C., Schweizer, J., 2013. An operational supporting tool for assessing wet-snow avalanche danger. Proceedings of the International Snow Science Workshop, Grenoble, Chamonix Mont-Blanc, 334—338. `https://arc.lib.montana.edu/snow-science/item.php?id=1860`.

Monti, F., Steinkogler, W., Mitterer, C., 2014. Livigno (Italy) Freeride project. Proceedings of the International Snow Science Workshop, Banff, Canada, 1066-–1070. `https://arc.lib.montana.edu/snow-science/item.php?id=2201`.

Monti, F., Mitterer, C., Steinkogler, W., Bavay, M., Pozzi, A., 2016. Combining snowpack models and observations for better avalanche danger assessments. Proceedings of the International Snow Science Workshop, Breckenridge, CO, USA, 343-–348. `https://arc.lib.montana.edu/snow-science/item.php?id=2290`.

Nagler, T., Rott, H., 2000. Retrieval of Wet Snow by Means of Multitemporal SAR Data. IEEE T. Geosci. Remote, 38, 754–765. 10.1109/36.842004.

Nagler, T., Rott, H., Ripper, E., Bippus, G., Hetzenecker, M., 2016. Advancements for snowmelt monitoring by means of Sentinel-1 SAR. Remote Sens., 8, 348. `https://doi.org/10.3390/rs8040348`.

Paloscia, S., Pettinato, S., Santi, E., Valt, M., 2017. Cosmo-skymed image investigation of snow features in alpine environment. Sensors, 17, 84. `https://doi.org/10.3390/s17010084`.

Patil, A., Singh, G., Rüdiger, C., 2020. Retrieval of snow depth and snow water equivalent using dual polarization SAR data. Remote Sens., 12, 1183. `https://doi.org/10.3390/rs12071183`.

Pettinato, S., Santi, E., Brogioni, M., Paloscia, S., Palchetti, E., Xiong, C., 2013. The potential of COSMO-SkyMed SAR images in monitoring snow cover characteristics. IEEE Geosci. Remote S., 10, 9—13. `https://doi.org/10.1109/LGRS.2012.2189752`.

Plattner, C.H., Braun, L.N., Brenning, A., 2004. Spatial variability of snow accumulation on Vernagtferner, Austrian Alps, in winter 2003/2004. Z. Gletscherkunde Glazialgeologie, 39, 43—57. `https://www.academia.edu/825084/Plattner_C_L_N_Braun_and_A_Brenning_2004_The_spatial_variability_of_snow_accumulation_on_Vernagtferner_Austrian_Alps_in_Winter_2003_2004_Zeitschrift_f%C3%BCr_Gletscherkunde_und_Glazialgeologie_39_43_57`.

Reppucci, A., Banque, X., Zhan, Y., Alonso, A., López-Martinez, C., 2012. Estimation of snow pack characteristics by means of polarimetric SAR data. Remote Sens. Agr. Ecosyst. Hydrol. XIV, 85310Z. `https://doi.org/10.1117/12.974598`.

Rott, H., Cline, D.W., Duguay, C., Essery, R., Etchevers, P., Hajnsek, I., Kern, M., MacElloni, G., Malnes, E., Pulliainen, J., Yueh, S.H., 2012. CoReH2O, a dual frequency radar mission for snow and ice observations. IEEE Int. Geosci. Remote S., 5550—5553. `https://doi.org/10.1109/IGARSS.2012.6352348`.

Rott, H., Scheiblauer, S., Wuite, J., Krieger, L., Floricioiu, D., Rizzoli, P., Libert, L., Nagler, T., 2021. Penetration of interferometric radar signals in Antarctic snow. The Cryosphere, 15, 4399—4419. `https://doi.org/10.5194/tc-15-4399-2021`.

Small, D., 2011. Flattening gamma: Radiometric terrain correction for SAR imagery. IEEE Trans. Geosci. Remote S., 49, 3081-–3093. `https://doi.org/10.1109/TGRS.2011.2120616`.

Snehmani, Singh, M.K., Gupta, R.D., Bhardwaj, A., Joshi, P. K., 2015. Remote sensing of mountain snow using active microwave sensors: a review. Geocarto Int., 30, 1—27. `https://doi.org/10.1080/10106049.2014.883434`.

Soncini, A., Bocchiola, D., 2011. Assessment of future snowfall regimes within the Italian Alps using general circulation models. Cold Reg. Sci. Technol., 68, 113—123. `https://doi.org/10.1016/J.COLDREGIONS.2011.06.011`.

Tsai, Y.L.S., Dietz, A., Oppelt, N., Kuenzer, C., 2019. Remote sensing of snow cover using spaceborne SAR: A review. Remote Sens., 11, 1456. `https://doi.org/10.3390/rs11121456`.

Tsang, L., Durand, M., Derksen, C., Barros, A.P., Kang, D.H., Lievens, H., Marshall, H.P., Zhu, J., Johnson, J., King, J., Lemmetyinen, J., Sandells, M., Rutter, N., Siqueira, P., Nolin, A., Osmanoglu, B., Vuyovich, C., Kim, E., Taylor, D., Merkouriadi, I., Brucker, L., Navari, M., Dumont, M., Kelly, R., Kim, R.S., Liao, T.H., Borah, F., Xu, X., 2022. Review article: Global monitoring of snow water equivalent using high-frequency radar remote sensing. The Cryosphere, 16, 3531—3573. `https://doi.org/10.5194/tc-16-3531-2022`.

Varsom Regobs, 2018. Snow observations. `https://regobs.no/?SelectedNumberOfDays=3&&NWLat=72.47527631092942&NWLon=-21.621093750000004&SELat=55.178867663282006&SELon=89.384765625` (accessed 1.13.25).

Velsand, P., 2017. Comparison and classification of an Arctic Transitional snow climate in Tromsø, Norway. `https://api.semanticscholar.org/CorpusID:134889729`.

Yommy, A. S., Liu, R., Wu, A. S., 2015. SAR image despeckling using refined Lee filter. 7th Int. C. Intel. Hum. Mach., Hangzhou, China, 260–265. `https://doi.org/10.1109/IHMSC.2015.236`.